Journal of Materials Chemistry A

COMMUNICATION

View Article Online
View Journal | View Issue

Cite this: J. Mater. Chem. A, 2019, 7, 1442

Received 6th November 2018
Accepted 3rd January 2019

DOI: 10.1039/c8ta10696g

rsc.li/materials-a

Cryo-TEM and electron tomography reveal leaching-induced pore formation in ZSM-5 zeolite†

Teng Li, ‡[a] Hanglong Wu,‡[bc] Johannes Ihli,[d] Zhiqiang Ma,[a] Frank Krumeich,[a] Paul H. H. Bomans,[bc] Nico A. J. M. Sommerdijk,[bc] Heiner Friedrich,[bc] Joseph P. Patterson*[bc] and Jeroen A. van Bokhoven *[ad]

Zeolites are the catalytic workhorses of the refinery and chemicals production industry. Their inherent micropores lead to remarkable shape-selectivity, but also present diffusion limitations on reactions. One scalable approach to further their functionality is to introduce mesopores into the individual zeolite crystal by base leaching. Using cryogenic transmission electron microscopy (cryo-TEM), we are able to capture the pore formation process in ZSM-5 zeolites in the solution state, first forming mesopores, to eventually yielding hollow crystals. Electron tomography indicates that the larger pores in the initial leaching stages tend to exist at the boundary between the aluminum-rich shell and the aluminum-poor core, while multiple small pores are also present within the aluminum-poor core. This indicates that pore formation is based on crystalline and chemical inhomogeneities at the single crystal level.

Zeolites are crystalline microporous aluminosilicates used in many chemical processes.[1–3] Their uniform microporous structures with molecular dimensions give rise to outstanding size and shape selectivity for guest molecules, thereby resulting in a wide interest in zeolite-based catalysts. However, the sole presence of such micropores always imposes diffusion limitations. One solution is employing hierarchical zeolite with meso/macropores introduced to allow faster guest molecule migration in the host frameworks.[4–7] For example, the lifetime of catalysts in the methanol-to-hydrocarbon (MTH) process can be increased by more than 3 times when mesopores are created.[8,9] Currently, encapsulating active metal clusters or nanoparticles into zeolites attracts intensive attention as it protects catalysts against sintering and enhances catalyst selectivity.[10] This confinement can be achieved either directly during zeolite synthesis,[11,12] or by post-synthetic methods.[13,14] For the post-synthetic methods, active metal species are typically encapsulated in the meso-/macropores.[15–20] Therefore, mesoporous or hollow zeolites with crystalline walls are excellent choices, with potential applications in drug delivery and catalysis.[21–23]

Due to a synthesis-inherent inhomogeneity in the aluminum and silicon distribution, hollow ZSM-5 zeolites can be prepared by simple base leaching.[24] Under mild base conditions and elevated temperature (such as in 0.15 M NaOH at 80 °C), the silicon-rich core is selectively dissolved, leaving a crystalline aluminum-rich shell. Understanding the mechanism of pore formation and its influence on the final structure is essential for the design of better catalysts and particle hosts. Previous transmission electron microscopy (TEM) studies on leached ZSM-5 have shown that the percentage of hollow crystals increases with time but that intermediate states are rarely observed.[25] Moreover, common characterization methods of pores such as gas physisorption can only provide average information on the mesopore volume in the bulk but not the information of local structure of pores in individual crystals. Consequently, the information about the initial pore formation and how the pore structure evolves with time in the native solution state, are still missing, potentially due to the common post-treatments after leaching, such as solid–liquid separation, drying and calcination. In contrast, time-resolved cryo-TEM analysis, which involves vitrification and thus examination of the reaction slurry itself, enable us to directly probe the processes in its natural state with remarkable spatial resolution (nanometer) and temporal resolution (<1 s).[26] Moreover, electron tomography with an automated ET data collection systems and high performance desktop computing provides a tool for the 3D structural characterization of inorganic material.[27]

ZSM-5 crystals were prepared by introducing tetrapropylammonium hydroxide (TPAOH) as the structure-directing

[a]ETH Zurich, Department of Chemistry and Applied Bioscience, Institute for Chemical and Bioengineering, Vladimir-Prelog-Weg 1, 8093 Zurich, Switzerland. E-mail: jeroen.vanbokhoven@chem.ethz.ch

[b]Eindhoven University of Technology, Laboratory of Materials and Interface Chemistry, Center of Multiscale Electron Microscope, PO Box 513, Eindhoven, The Netherlands. E-mail: patters3@uci.edu

[c]Institute for Complex Molecular Systems, Eindhoven University of Technology, PO Box 513, Eindhoven, The Netherlands

[d]Paul Scherrer Institute, 5232 Villigen, Switzerland

† Electronic supplementary information (ESI) available. See DOI: 10.1039/c8ta10696g

‡ These authors contribute equally to this work.

agent (SDA) that was removed by calcination at 550 °C.[28] The resulting zeolite crystals have a Si/Al ratio of ~59, determined by atomic absorption spectroscopy. Powder X-ray diffraction confirmed the MFI-type structure (Fig. S1a†). ^{27}Al MAS NMR indicated that all the aluminum is in tetrahedral coordination (Fig. S1b†). Cryo-TEM analysis shows a range of morphologies, including pristine crystals (on average 94 nm × 78 nm × 50 nm coffin-like shape) as well as smaller and more spherical particles (Fig. S2†).

Base leaching experiments were performed at 50 °C and 80 °C. In general, 1 g of the zeolite was suspended in deionized water, transferred to a Teflon reactor and stirred at the leaching temperature for 20 minutes. A sodium hydroxide solution was subsequently added to give the desired base concentration, 0.3 M for 50 °C, and 0.15 M for 80 °C. The addition of the basic solution was considered as time zero. 3 μL aliquots were taken from the reactor at 15 minute intervals and quickly vitrified in liquid nitrogen to achieve a fast freezing of samples. During vitrification, the temperature in the chamber of the vitrobot was kept at 60 °C and the humidity was maintained close to 100%. The reactor was closed tightly during the whole process except at the time of sampling. The dissolution kinetics were determined at 80 °C by measuring the weight loss of original samples *versus* time, indicating that >90% of the leaching occurs within the first 50 min (Fig. S3†). However, the rapid dissolution process hinders the capturing earlier stages using time-resolved sampling. Leaching at 50 °C slowed down the dissolution, thus increasing the possibility of capturing distinct and observable stages in the pore formation process (see ESI†).

Fig. 1 shows typical cryo-TEM images collected during the leaching process at 80 °C (a–e) and 50 °C (f–j). In general, even for the slower leaching kinetics the initiation of leaching appears to be slower than the progression, such that in various time-points mixtures of pristine, partially leached, and fully leached particles can be observed. While this makes determination of the exact leaching process difficult, there are clearly observable general stages when looking at the sample as a whole. After 15 minutes at 80 °C, mesopores had appeared in most crystals, being randomly distributed (Fig. 1b and c). These pores appear to develop into cavities while the shells mostly remained intact with extended leaching (Fig. 1d and e). When comparing cryo-TEM results with the observations from conventional TEM on the same zeolite system,[25] cryo-TEM can make a difference, as it shows that hollow structures originate from the expansion and coalescence of multiple mesopores, which we were not able to see from the conventional TEM.

At 50 °C, zeolites with mesopores, though as a minority, started to appear after 30 minutes. Fig. 1g displays a representative crystal in which a discernible closed large pore is near the rim, and Fig. S4† shows many crystals with similar pores. Even for crystals that suffer from shell damage, pores extend to the outer edge, situated in a similar position – close to the rim. With extended leaching more pores appeared within individual crystals, and such pores were no longer confined to the rim but randomly dispersed inside the crystal (Fig. 1h). Pore-to-pore connections can be often observed, leading to a quasi-hollow structure (Fig. 1i). Ultimately, after one day, crystals with an empty core structure appeared (Fig. 1j and S5†).

To further investigate the location of the pores during the early stages of leaching, we performed electron tomography (Movie S1†). The crystals were leached, and then quickly centrifuged to separate them from the liquid. The absence of liquid improved the resolution of the tomography images, although this operation somewhat prolonged the dissolution. Fig. 2 shows the slices through different planes of the particles after alignments of the tilt series and tomography reconstruction (Movies S2 and S3†). The first pores appeared not only close to the rim of the crystal (Fig. 2a) but also in other areas of the particle core (Fig. 2 and S16†). Mesopores of larger size were preferentially located close to the rim as confirmed by 3D reconstruction (Movie S4, Fig. S21†), which is consistent with the cryo-TEM observations. Interestingly, in the 3D reconstruction, we also noticed that the surface of the large pore phase (close to the particle edge) is quite flat, which seems to be parallel with {010} facets (Fig. S22†), suggesting that the leaching is prohibited from penetrating further into the rim.

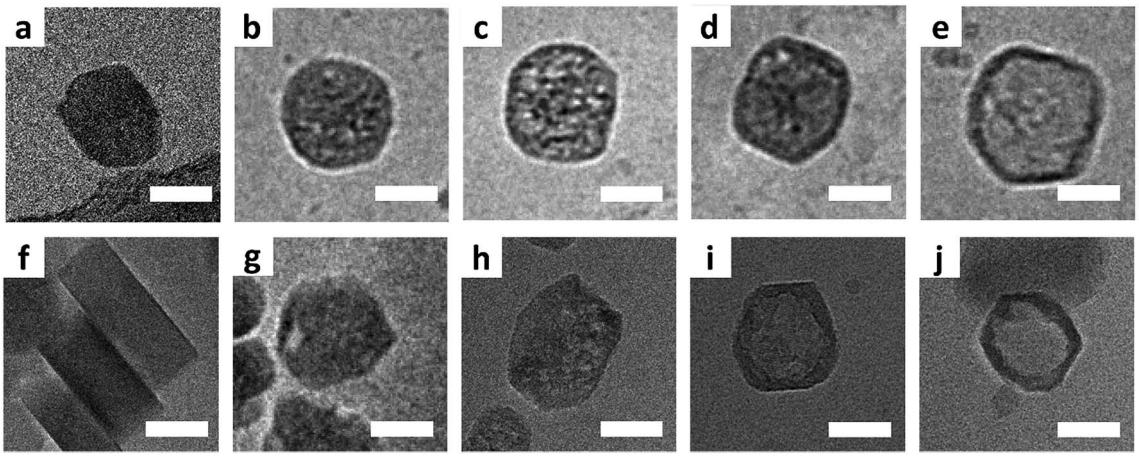

Fig. 1 Top: Cryo-TEM images of particles with typical features leached at 80 °C for (a) pristine crystal, (b, c) mesoporous crystal, (d, e) hollow crystal. Bottom: Cryo-TEM images of particles leached at 50 °C for (f) pristine, (g–i) mesoporous crystal, (j) hollow crystal. Scale bars are 50 nm.

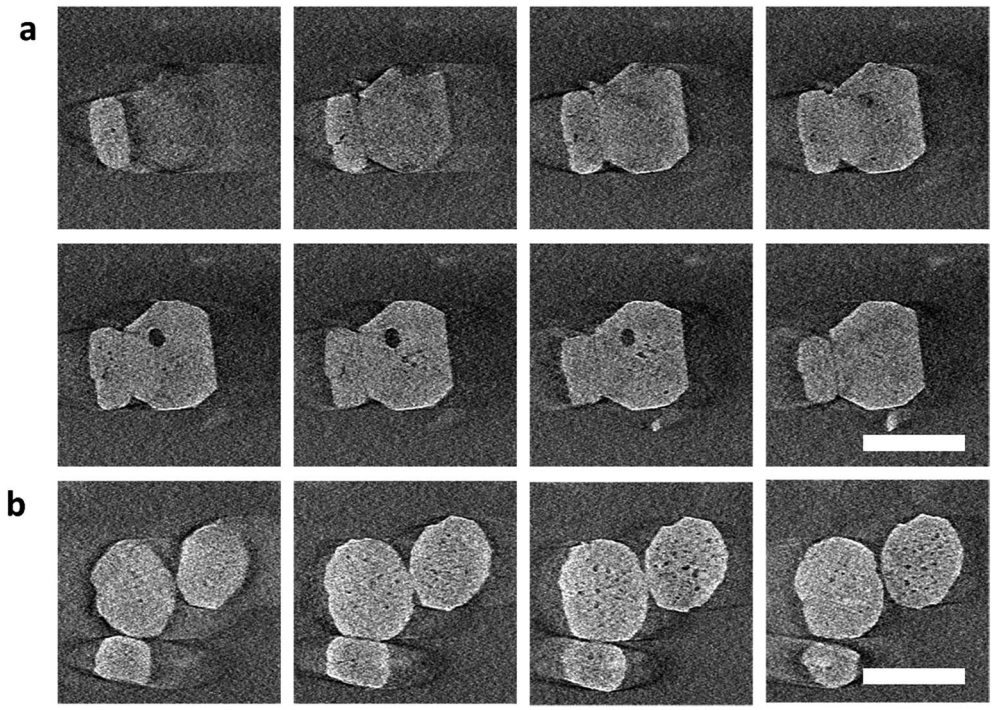

Fig. 2 Gallery of z-slices showing different cross sections of 3D reconstruction of the particles cropping out from different areas in Fig. S16(d–i)† in the early-stage leaching process. (a) is cropped out from area A and (b) from area B. The zeolite nanoparticles (~100 nm in size) are leached for 30 min at 40 °C. Electron flux: 150 e per nm^2 per s, 100 e per nm^2 per image. Scale bar: 100 nm. A more detailed vision refers to Movies S2 and S3.†

Particle dimension analysis shows no significant changes in overall size or shape of the crystals over the leaching process (Fig. S6†), indicating the leaching mainly affects the particle interior. Crystals with different morphology categories are observed, including pristine crystals, crystals with the larger pore in the rim and small pore in the core, crystals with pores connected with each other and hollow zeolite crystals (Fig. S19†). From the pristine sample, a crystal appears to either undergo dissolution to form closed pores inside, or to lose part of the rim. Some crystals display larger pore structures at intermediate stages, later forming a structure with an empty core and an intact rim (Scheme 1). For other crystals the shells were destroyed with further leaching. Such observations explain the appearance of hollow zeolite crystals and a continuous rise in the percentage of crystals with open pores at the late stage (Fig. S7†).

The preferential dissolution of the core relates to the compositional or crystalline inhomogeneity within individual crystals. The feature of aluminum zoning for the pristine crystals is confirmed by energy-dispersive X-ray spectroscopy (EDX) mapping (Fig. S8†).[28] However, due to the low aluminum content and small crystal size, a direct EDX measurement cannot provide quantitative and detailed chemical gradient through the whole crystal (Fig. S9†). Based on the same synthesis procedure, a somewhat larger ZSM-5 crystal (400 nm × 350 nm × 220 nm) was prepared by only increasing the water content in the mother gel. These large crystals show properties similar to the aforementioned sample, where after base leaching, similar hollow crystals are obtained (Fig. S10†), and leaching at 50 °C also leads to the formation of relatively larger pores, initially located close to the rim initially (Fig. S11†). The shell ratio of hollow crystals, *i.e.* the ratio between the shell

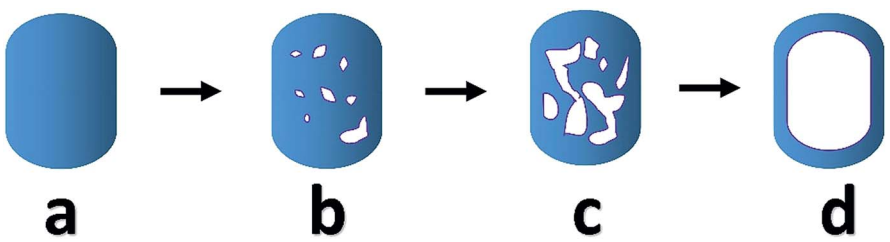

Scheme 1 The evolution of pore structure for zeolite crystals during base leaching. (a) Pristine crystal (b) crystal with larger pores near the rim and smaller pores in the core (c) coalescence and connection of different mesopores (d) hollow crystal. Note that the 3D structure of crystal is simplified into a 2D mode.

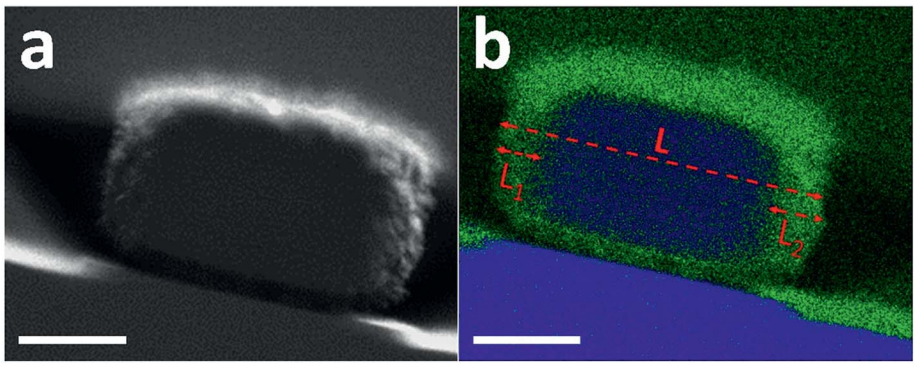

Fig. 3 Secondary electron STEM image (a) and the corresponding EDX map (b) of the cross section of a large ZSM-5 crystal. Scale bars: 100 nm. The cross section of the crystal was prepared by gallium focus ion beam milling. The sharp contrast on the top was due to Pt coating. For EDX mapping, blue and green colors stand for silicon and aluminum respectively. The ratio of aluminum-rich area/the length of cross section, *i.e.* (*L*1 + *L*2)/*L*, equals to 30%.

thickness and the crystal size, was on average 15%. Fig. 3a displays the cross section of one large crystal that was prepared by Focus Ion Beam (FIB) milling (Fig. S12†). The front and rear ends were removed and only the middle cross section with a thickness of 200 nm was kept and analyzed by STEM-EDX. Aluminum was concentrated in the rim while little aluminum was found in the inner part (Fig. 3b and S13†). The aluminum-rich area accounts for nearly 30% of the cross section, which corresponds to twice of the shell ratio of leached hollow crystals. This consistency indicates the role of aluminum zoning in the formation of hollow ZSM-5 crystals.

Knowing the location of defects in zeolite crystals is important since it may have practical consequences.[29,30] For example, Barbera *et al.* pointed out that the internal framework defects are crucial for the deactivation of the ZSM-5 catalysts in the conversion of methanol to hydrocarbons (MTH) since coking at the inner defects leads to a more pronounced deactivation.[29] Interestingly, although pore formation commenced throughout the whole aluminum-poor core (Fig. 2 and S16†), the mesopores of larger size firstly formed in an area close to the rim, suggesting a lower stability in this area. We also confirmed that the interface between the aluminum-rich and the aluminum-poor parts of the individual crystals is exactly where such pores are formed (Fig. S14†). The significant size difference between the larger interfacial pores and the smaller pores distributed throughout the particles indicate two different formation mechanisms. Furthermore, typically only one interfacial pore is observed per particle, whereas multiple smaller pores are observed in all particles analyzed by tomography. Consequently, we propose that interfacial pore formation occurs *via* slow nucleation and fast growth and core pore formation occurs *via* fast nucleation and slow growth. More specifically, during leaching mesopore nuclei appear in the core area and coalesce with other pores to form big ones. The origin of this difference may be the strain in that area where two parts of the crystal with slightly different bond distances and angles – due to the different aluminum content – meet. The eventual preservation of the shell is mainly due to a higher concentration of aluminum in the rim.[28] The negative charge of the AlO_4-tetrahedra makes the rim more resistant to hydrolysis compared to the core. Consequently, the hollow structure results from selective removal of the silicon-rich inner part. At the end of the leaching process, we also observed crystals without hollow structure. The diversity of pore formation indicates that different crystals possess different properties, either in composition and/or structure.[25]

Conclusion

Overall, time-resolved cryo-TEM analysis and electron tomography revealed the pore evolution in the native solution state and the 3D pore distribution in the early leaching stage. Most importantly, we found the dissolution commences in the silica-rich core, and the larger mesopores form preferentially at the interface between the aluminum-rich and the aluminum-poor part, while multiple small pores also present within the aluminum-poor core. Different leaching behaviors were observed in the same batch, which indicates different compositional and/or structural properties over single crystals. The insight into the initial pore formation in zeolite leaching that our work provides advances our understanding of the pore structure engineering in zeolites to design better catalysts and particle hosts.

Conflicts of interest

The authors declare no conflict of interest.

Acknowledgements

We thank the Swiss National Science Foundation (SNF) for the support of the work of L. T. and I. J. (153556). L. T. thanks the China Scholarship Council (CSC) for the financial support. W. H. is supported by the EU H2020 Marie Sklodowska-Curie Action project "MULTIMAT". J. P is supported by the EU H2020 Marie Sklodowska-Curie Action project "LPEMM". Electron microscopy work was performed at the Scientific Centre for Optical and Electron Microscopy (ScopeM) ETH Zürich and Eindhoven University of Technology. We thank Laura Hazendonk and Claudia Muniz Ortera (Eindhoven University of

Technology, The Netherlands) for the help with the reconstructions and visualization of electron tomography. We thank Dr Ana Pinar for helpful discussion.

References

1 A. Corma and A. Martinez, *Adv. Mater.*, 1995, **7**, 137–144.
2 J. Shi, Y. Wang, W. Yang, Y. Tang and Z. Xie, *Chem. Soc. Rev.*, 2015, **44**, 8877–8903.
3 B. M. Weckhuysen and J. Yu, *Chem. Soc. Rev.*, 2015, **44**, 7022–7024.
4 Y. Tao, H. Kanoh, L. Abrams and K. Kaneko, *Chem. Rev.*, 2006, **106**, 896–910.
5 J. Pérez-Ramírez, C. H. Christensen, K. Egeblad, C. H. Christensen and J. C. Groen, *Chem. Soc. Rev.*, 2008, **37**, 2530–2542.
6 A. N. van Laak, S. L. Sagala, J. Zečević, H. Friedrich, P. E. de Jongh and K. P. de Jong, *J. Catal.*, 2010, **276**, 170–180.
7 K. P. de Jong, J. Zečević, H. Friedrich, P. E. de Jongh, M. Bulut, S. Van Donk, R. Kenmogne, A. Finiels, V. Hulea and F. Fajula, *Angew. Chem.*, 2010, **122**, 10272–10276.
8 J. Kim, M. Choi and R. Ryoo, *J. Catal.*, 2010, **269**, 219–228.
9 L. Wu, V. Degirmenci, P. C. Magusin, N. J. Lousberg and E. J. Hensen, *J. Catal.*, 2013, **298**, 27–40.
10 D. Farrusseng and A. Tuel, *New J. Chem.*, 2016, **40**, 3933–3949.
11 M. Choi, Z. Wu and E. Iglesia, *J. Am. Chem. Soc.*, 2010, **132**, 9129–9137.
12 N. Wang, Q. Sun, R. Bai, X. Li, G. Guo and J. Yu, *J. Am. Chem. Soc.*, 2016, **138**, 7484–7487.
13 S. Li, A. Tuel, F. Meunier, M. Aouine and D. Farrusseng, *J. Catal.*, 2015, **332**, 25–30.
14 C. Dai, X. Li, A. Zhang, C. Liu, C. Song and X. Guo, *RSC Adv.*, 2015, **5**, 40297–40302.
15 A. W. Petrov, D. Ferri, F. Krumeich, M. Nachtegaal, J. A. van Bokhoven and O. Kröcher, *Nat. Commun.*, 2018, **9**, 2545.
16 A. B. Laursen, K. T. Højholt, L. F. Lundegaard, S. B. Simonsen, S. Helveg, F. Schüth, M. Paul, J. D. Grunwaldt, S. Kegnæs and C. H. Christensen, *Angew. Chem.*, 2010, **122**, 3582–3585.
17 D. Fodor, T. Ishikawa, F. Krumeich and J. A. van Bokhoven, *Adv. Mater.*, 2015, **27**, 1919–1923.
18 S. Li, A. Tuel, J. L. Rousset, F. Morfin, M. Aouine, L. Burel, F. Meunier and D. Farrusseng, *ChemNanoMat*, 2016, **2**, 534–539.
19 C. Dai, A. Zhang, L. Luo, X. Zhang, M. Liu, J. Wang, X. Guo and C. Song, *Catal. Today*, 2017, **297**, 335–343.
20 D. Laprune, A. Tuel, D. Farrusseng and F. Meunier, *Appl. Catal., A*, 2017, **535**, 69–76.
21 N. Ren, A.-G. Dong, W.-B. Cai, Y.-H. Zhang, W.-L. Yang, S.-J. Huo, Y. Chen, S.-H. Xie, Z. Gao and Y. Tang, *J. Mater. Chem.*, 2004, **14**, 3548–3552.
22 D. Wang, G. Zhu, Y. Zhang, W. Yang, B. Wu, Y. Tang and Z. Xie, *New J. Chem.*, 2005, **29**, 272–274.
23 C. Pagis, A. R. Morgado Prates, D. Farrusseng, N. Bats and A. Tuel, *Chem. Mater.*, 2016, **28**, 5205–5223.
24 D. Fodor, L. Pacosová, F. Krumeich and J. A. van Bokhoven, *Chem. Commun.*, 2014, **50**, 76–78.
25 D. Fodor, F. Krumeich, R. Hauert and J. A. van Bokhoven, *Chem.–Eur. J.*, 2015, **21**, 6272–6277.
26 J. P. Patterson, Y. Xu, M.-A. Moradi, N. A. Sommerdijk and H. Friedrich, *Acc. Chem. Res.*, 2017, **50**, 1495–1501.
27 H. Friedrich, P. E. de Jongh, A. J. Verkleij and K. P. de Jong, *Chem. Rev.*, 2009, **109**, 1613–1629.
28 T. Li, Z. Ma, F. Krumeich, A. J. Knorpp, A. B. Pinar and J. A. Van Bokhoven, *ChemNanoMat*, 2018, **4**, 992–999.
29 K. Barbera, F. Bonino, S. Bordiga, T. V. Janssens and P. Beato, *J. Catal.*, 2011, **280**, 196–205.
30 S. Svelle, L. Sommer, K. Barbera, P. N. Vennestrøm, U. Olsbye, K. P. Lillerud, S. Bordiga, Y.-H. Pan and P. Beato, *Catal. Today*, 2011, **168**, 38–47.

